CM²
MAGAZINE

第 122 期

创刊词

海洋是生命的摇篮，是文明的纽带。地球上最早的生命诞生于海洋，海洋里的生命最终进化成了人类，人类的文化融合又通过海洋得以实现。人因海而兴。

人类对海洋的探索从未停止。从远古时代美丽的神话传说，到麦哲伦的全球航行，再到现代对大洋的科学钻探计划，海洋逐渐从人类敬畏崇拜幻想的精神寄托演变成可以开发利用与科学研究的客观存在。其中，上个世纪与太空探索同步发展的大洋科学钻探计划将人类对海洋的认知推向了崭新的纬度：深海（deep sea）与深时（deep time）。大洋钻探计划让人类知道，奔流不息的大海之下，埋藏的却是亿万年的地球历史。它们记录了地球板块的运动，从而使板块构造学说得到证实；它们记录了地球环境的演变，从而让古海洋学方兴未艾。

在探索海洋的悠久历史中，从大航海时代的导航，到大洋钻探计划中不可或缺的磁性地层学，磁学发挥了不可替代的作用。这不是偶然，因为从微观到宏观，磁性是最基本的物理属性之一，可以说，万物皆有磁性。基于课题组的学科背景和对海洋的理解，我们对海洋的探索以磁学为主要手段，海洋磁学中心因此而生。

海洋磁学中心，简称 CM^2，一为其全名"Centre for Marine Magnetism"的缩写，另者恰与爱因斯坦著名的质能方程 $E = MC^2$ 对称，借以表达我们对科学巨匠的敬仰和对科学的不懈追求。

然而科学从来不是单打独斗的产物。我们以磁学为研究海洋的主攻利器，但绝不仅限于磁学。凡与磁学相关的领域均是我们关注的重点。为了跟踪反映国内外地球科学特别是与磁学有关的地球科学领域的最新研究进展，海洋磁学中心特地主办 CM^2 Magazine，以期与各位地球科学工作者相互交流学习、合作共进！

"海洋孕育了生命，联通了世界，促进了发展"。21 世纪是海洋科学的时代，由陆向海，让我们携手迈进中国海洋科学的黄金时代。

目录

1. 更新世时期非洲西北部水文气候与植被的驱动因素

翻译人：仲义 zhongy@sustech.edu.cn

摘要：碳热带草原生态系统是人类进化过程的重要栖息场所，对现今撒哈拉以南非洲地区粮食安全至关重要，但是这些生态系统中气候和生态的根本驱动因素仍然不是很清楚。本文作者利用植被中蜡同位素和粉尘通量来追踪非洲西北部季风潜在的控制机制，并评估生态系统对季风降雨和大气二氧化碳变化的响应关系。研究表明，季风降雨受到低纬度日晒量梯度控制，同时降水的升高与草原向沙漠地区不断扩张有关，而大气 CO_2 变化主要驱动了热带草原生态系统的 C3/C4 的组成。

ABSTRACT: Savanna ecosystems were the landscapes for human evolution and are vital to modern Sub-Saharan African food security, yet the fundamental drivers of climate and ecology in these ecosystems remain unclear. Here we generate plant-wax isotope and dust flux records to explore the mechanistic drivers of the Northwest African monsoon, and to assess ecosystem responses to changes in monsoon rainfall and atmospheric $p\text{CO}_2$. We show that monsoon rainfall is controlled by low-latitude insolation gradients and that while increases in precipitation are associated with expansion of grasslands into desert landscapes, changes in $p\text{CO}_2$ predominantly drive the C3/C4 composition of savanna ecosystems.
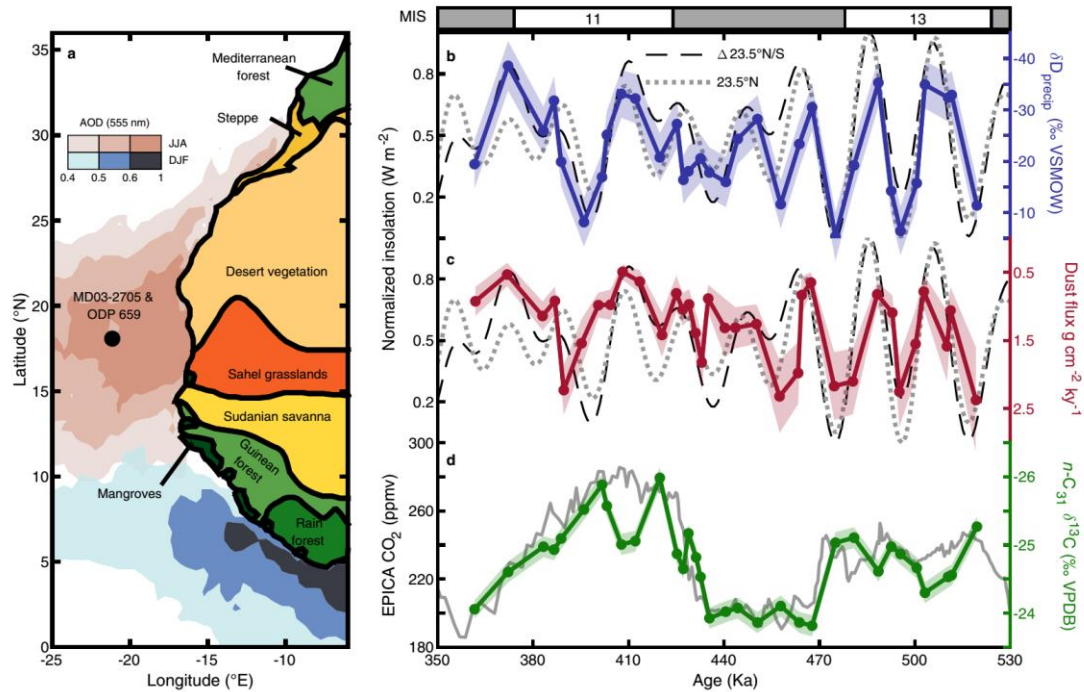
Figure 1. Regional context and new records of monsoon rainfall, dust, and vegetation. a Map of Northwest Africa with biome distributions on land ref. 54, the aerosol optical depth (AOD, 555 nm) (summer: JJA and winter: DJF, 2000–2017) over the ocean (Giovanni, NASA EarthData) showing the location of the modern summer and winter Saharan dust plumes (colorbar, ref. 127), the core location for MD03-2705 and ODP 659 is labeled with a black circle b δDprecip with 1 σ uncertainty plotted with June 21 23.5°N insolation (dotted line, r = −0.77) and the summer inter-hemispheric insolation gradient June 21 23.5°N–23.5°S (dashed line, r = −0.76), insolation was determined using ref. 126 and normalized to values between 0 and 1. c 3HeET-normalized dust flux plotted with insolation curves as in a (23.5°N, r = −0.46; Δ23.5°N/S, r = −0.50). d Plant-wax C31 n-alkane δ13C with 1 σ uncertainty plotted with EPICA ice core CO2 concentration ref. 128 (r = –0.81). δDprecip and 3HeET-normalized dust flux are also well correlated (r = 0.68). All correlation coefficients are significant at a p value of <0.01. Marine isotope stages (MIS) are indicated with interglacials periods shown in white and glacial periods in gray

2. 岩浆流动速率预测玄武质火山喷发

翻译人：周洋 zhouy3@sustech.edu.cn

摘要：预测火山爆发是火山学的最大挑战。虽然在提前数小时到数天火山喷发预测方面取得了一些突破，但在更长时间范围内进行可靠的预测仍然存在很大挑战。我们研究表明，源自地表变形的岩浆流动速率是玄武质火山喷发的指标。在所有评估的案例中，流动速率≥0.1 $km^3\,yr^{-1}$ 时， 1 年内岩浆发生流动和喷发，而流动速率 <0.01 $km^3\,yr^{-1}$ 时，在 89% 的情况下，不会导致岩浆喷发。我们可以用粘弹性模型解释这些行为，其中松弛时间尺度控制岩墙扩张的临界超压。因此，虽然表面变形本身是火山喷发的微弱前兆，但估算玄武质岩浆流动速率可以改进预测，大大提高前几周到几个月火山喷发预测的能力。

ABSTRACT: Forecasting eruption is the ultimate challenge for volcanology. While there has been some success in forecasting eruptions hours to days beforehand, reliable forecasting on a longer timescale remains elusive. Here we show that magma inflow rate, derived from surface deformation, is an indicator of the probability of magma transfer towards the surface, and thus eruption, for basaltic calderas. Inflow rates ≥0.1 km3 yr−1 promote magma propagation and eruption within 1 year in all assessed case studies, whereas rates <0.01 km3 yr−1 do not lead to magma propagation in 89% of cases. We explain these behaviours with a viscoelastic model where the relaxation timescale controls whether the critical overpressure for dyke propagation is reached or not. Therefore, while surface deformation alone is a weak precursor of eruption, estimating magma inflow rates at basaltic calderas provides improved forecasting, substantially enhancing our capacity of forecasting weeks to months ahead of a possible eruption.
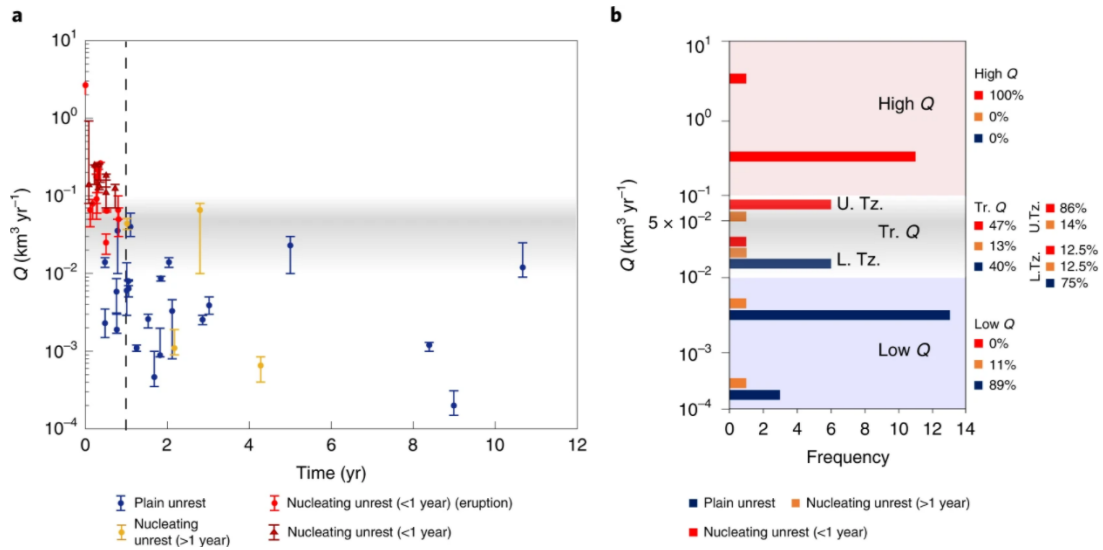
Figure 1. Global a, Duration of unrest and corresponding inflow rate, Q, as a function of unrest outcome. The grey area highlights the zone with transitional rates ($5 \pm 4 \times 10^{-2}$ km3 yr−1). The vertical dashed grey line separates the unrest episodes lasting <1 year from those lasting >1 year. Data are reported with the confidence limits (error bars). b, Histogram of frequency of the injected rates. Tr. Q, L. Tz. and U. Tz. refer to transitional, lower transitional and upper transitional rates, respectively. Background colours: blue=Low Q, grey=Transitional Q, red=High Q.

3. 二元同位素温度测定法反映新生代深海温度演化

翻译人：张琪 zhangq7@sustech.edu.cn

摘要：认识以往的气候状态对于我们理解持续的温室气体排放对未来气候的影响至关重要。本文，作者使用二元同位素温度测定法，重新审视了过去 6500 万年来深海温度的基准时间序列。本文来自大西洋深处估算所得的温度总体上比基于氧同位素重建的温度高得多，这凸显了深海 pH 值和（或）海水氧同位素组成变化对新生代典型氧同位素记录的可能影响。此外，本文数据显示，在早期始新世急性温室暖期，深海温度出现了以前未被认识到的巨大波动。本文的结果呼吁学者重新评估新生代海洋温度的历史，以期更准确的理解构造事件和变化的温室效应对气候的响应。

ABSTRACT: Characterizing past climate states is crucial for understanding the future consequences of ongoing greenhouse gas emissions. Here, we revisit the benchmark time series for deep ocean temperature across the past 65 million years using clumped isotope thermometry. Our temperature estimates from the deep Atlantic Ocean are overall much warmer compared with oxygen isotope–based reconstructions, highlighting the likely influence of changes in deep ocean pH and/or seawater oxygen isotope composition on classical oxygen isotope records of the Cenozoic. In addition, our data reveal previously unrecognized large swings in deep ocean temperature during early Eocene acute greenhouse warmth. Our results call for a reassessment of the Cenozoic history of ocean temperatures to achieve a more accurate understanding of the nature of climatic responses to tectonic events and variable greenhouse forcing.
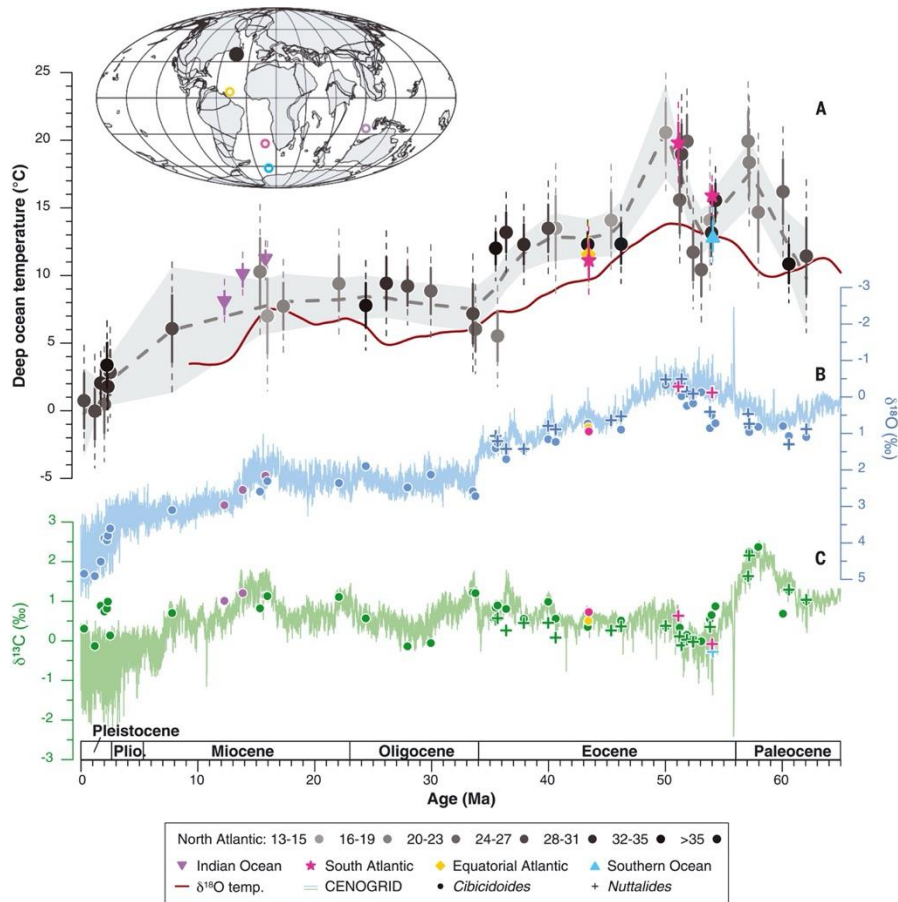
Figure 1. Clumped isotope–based reconstruction of deep ocean temperatures compared with classical foraminifera isotope records. (A) Δ_{47} temperatures from the North Atlantic (gray symbols) compared with estimates from other sites (colored symbols; see inset map) in the Indian Ocean, equatorial and South Atlantic, and the Atlantic sector of the Southern Ocean. The early Eocene data from (18) span a time interval of ~200,000 years and were combined into one data point for each location. Error bars for Δ_{47} temperatures are 68% (solid lines) and 95% (stippled lines) confidence intervals. For the North Atlantic data, darkness of shading reflects robustness based on degree of replication, with ranges of replicate numbers specified in the figure legend. The other data points are based on 51 to >200 measurements (see data S1) reflected in the size of the error bars. The gray stippled line is a LOESS fit through the North Atlantic data with a Monte Carlo–based 95% confidence interval (see the supplementary materials), and is meant as visual guidance rather than as an alternative representation of the data. The red line is a previous estimate of deep ocean temperature based on $\delta^{18}O_b$ and sea-level reconstructions (6). (B) CENOGRID $\delta^{18}O_b$ record (2) and $\delta^{18}O_b$ results from species of the genus Cibicidoides (circles) and Nuttalides (crosses) from the clumped isotope analyses, corrected for interspecies offsets (Cibicidoides: +0.64‰; Nuttalides:

6

+0.4‰). (C) CENOGRID δ13C record (2) with results from Cibicidoides and Nuttalides species from the clumped isotope analyses. Note that the global CENOGRID record also includes corrections for offsets between sites and ocean basins, which we do not apply to our data. Typical offsets in $\delta^{18}O_b$ between Atlantic and Pacific sites (the latter interpreted as equivalent to global) are on the order of –0.2 to –0.3‰ for the Eocene to Oligocene (2), compared with 0 to –0.5‰ offsets in our Nuttalides data. Inset map shows site locations on a paleogeographic reconstruction for ~50 Ma (www.odsn.de/odsn/services/paleomap/paleomap.html). Also see fig. S4 for close-up views of early and late Cenozoic interval data.
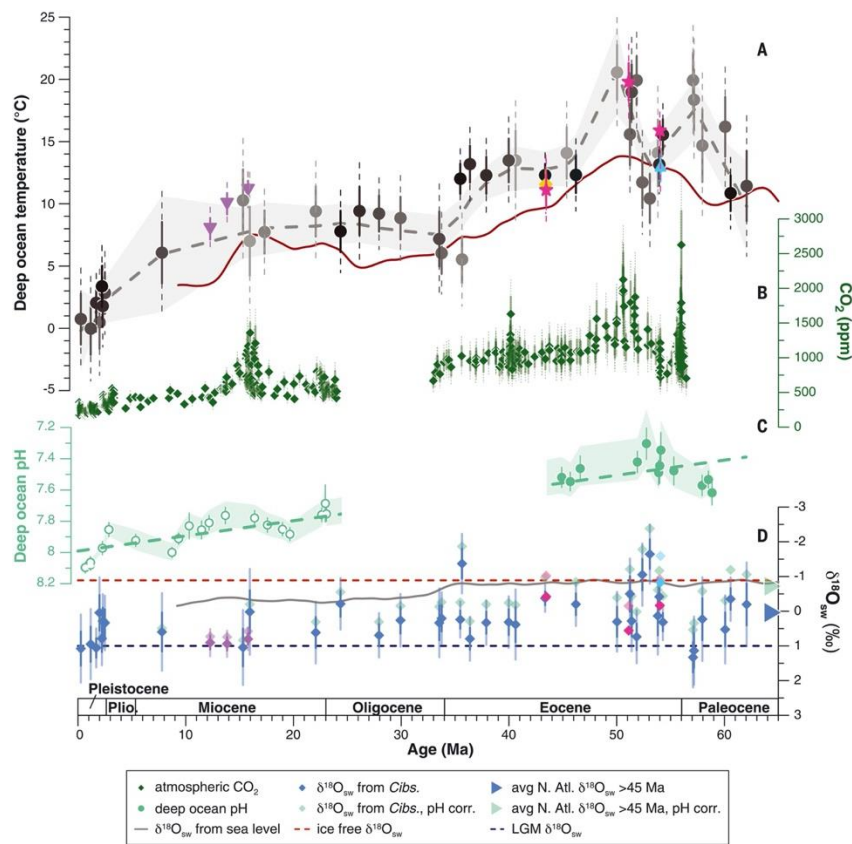
Figure 2. Cenozoic evolution of seawater isotopic composition and comparison with changes in the carbon cycle. (A to C) Δ_{47} temperatures as in Fig. 1 (A) with atmospheric CO_2 concentration from boron isotopes in planktic foraminifera (24) with 1 and 2 SD (stippled lines) uncertainties (B), and reconstructed deep ocean pH from boron isotopes in benthic foraminifera [(40), open symbols; this study, closed symbols] with linear regression (C). Error bars show the influence of uncertainties in δ11B and temperature at 2 SDs and the shaded area reflects the influence of $\delta^{11}B_{sw} \pm 0.5$‰ (see the materials and methods). (D) Calculated $\delta^{18}O_{sw}$ (against the SMOW standard; blue/purple symbols

7

with 68 and 95% confidence intervals) compared with suggested "ice-free" $\delta^{18}O_{sw}$ of –0.9 ‰ [red stippled line; (6)], $\delta^{18}O_{sw}$ of Pleistocene glacial periods of 1‰ (dark blue stippled line), and $\delta^{18}O_{sw}$ reconstructed from sea-level estimates and the estimated ice-free $\delta^{18}O_{sw}$ [gray line; (6)]. Blue data points are from the North Atlantic, and other colors reflect other sites (see Fig. 1). Light green and other faded color symbols are $\delta^{18}O_{sw}$ estimates after correcting $\delta^{18}O_b$ for the long-term increase in deep ocean pH (regression line in C) and assuming a sensitivity of 1.42 ‰ per pH unit (26). Although this first-order correction does not eliminate the variability in $\delta^{18}O_{sw}$, it brings the values on |average in closer agreement with the estimated ice-free $\delta^{18}O_{sw}$ for the early part of the record. Arrows on the right show the average North Atlantic $\delta^{18}O_{sw}$ values for >45 Ma before (blue) and after (light green) pH correction.

4. 南海洋壳玄武岩异常的 δ^{26}Mg 值

翻译人：刘伟 inewway@163.com

摘要：洋壳玄武岩是否受到板块俯冲的影响一直是人们争论的热点问题。南海是西太平洋最大的边缘盆地之一，被太平洋板块和印度板块的俯冲所包围。但由于缺乏海底火成岩地壳玄武岩的取样，迄今为止在盆地的火山地球化学研究中没有明确的俯冲证据。IODP 349 航次获取了位于南海东部次海盆(Site U1431)和西南次海盆(Site U1433 和 U1434)的残余扩张脊附近的海底玄武岩岩心。回收的玄武岩样品指示了含辉石的橄榄岩地幔源。本文报道了其中 14 个大洋地壳玄武岩样品的镁同位素数据。3 个孔大部分玄武岩的 δ^{26}Mg 值高于地幔的平均值(-0.25‰)，高达-0.10‰。δ^{26}Mg 与岩浆作用的地球化学指标(MgO、CaO/Al$_2$O$_3$、La/Sm、Nb/Zr)没有相关性，表明结晶分馏和部分熔融作用对南海玄武岩 Mg 同位素组成的影响不明显。因此，镁同位素的变化具有地幔源的特征。考虑到 Ce/Pb 值变化较大，^{87}Sr/^{86}Sr 值升高，而 ^{143}Nd/^{144}Nd 值呈地幔特征，认为 δ^{26}Mg 值的变化可能是俯冲释放流体的交代作用所致。Mg 和 Sr-Fe 同位素的耦合作用表明，南海玄武岩的高-δ^{26}Mg 值是由含辉石的橄榄岩地幔、附近的海南地幔柱物质和俯冲的蛇纹岩释放流体混合形成的。因此，这些 Mg 同位素表明南海玄武岩的地幔源受俯冲物质的影响，为南海板块俯冲过程中的初始扩张、形成和演化提供了进一步的证据。

ABSTRACT: Whether or not oceanic crust basalts are affected by plate subduction is a hot topic of debate. The South China Sea is one of the largest marginal basins in the western Pacific Ocean and has been surrounded by subduction of the Pacific plate and Indian plate, yet, to date, no study has clearly shown evidence of subduction in the geochemistry of volcanism in the basin due to a lack of sampling of igneous crust basalts on the seafloor. The International Ocean Discovery Program Expedition 349 cored seafloor basalts near the fossil spreading ridges of the eastern (Site

U1431) and southwestern (Site U1433 and U1434) subbasins in the South China Sea. The recovered basalt samples indicated a pyroxenite-bearing peridotite mantle source. Here, we report Mg isotopic data from 14 of these oceanic crust basalt samples. The $\delta^{26}Mg$ values of most basalts from the three drill holes were higher (up to $-0.10‰$) than that of the average mantle ($-0.25‰$). The lack of correlations of $\delta^{26}Mg$ with geochemical indices of magmatic processes (e.g., MgO, CaO/Al_2O_3, La/Sm, Nb/Zr) suggests that crystal fractionation and partial melting had insignificant effects on the Mg isotopic compositions of the South China Sea basalts. Thus, the variations in Mg isotopes were inherited from their mantle sources. Considering the highly varied Ce/Pb ratios and elevated $^{87}Sr/^{86}Sr$ values but mantle-like $^{143}Nd/^{144}Nd$ values, we propose that the varied $\delta^{26}Mg$ values were likely caused by metasomatism of subduction-released fluids. The coupling of Mg and Sr-Fe isotopes provides robust evidence that the high-$\delta^{26}Mg$ values of the South China Sea basalts resulted from mixing among pyroxenite-bearing peridotite mantle, the nearby Hainan plume materials, and subducting serpentinite-released fluids. Therefore, these Mg isotopes suggest that the mantle source of the South China Sea basalts was influenced by subducted materials, providing further evidence of the initial expansion, formation, and evolution of the South China Sea during plate subduction.
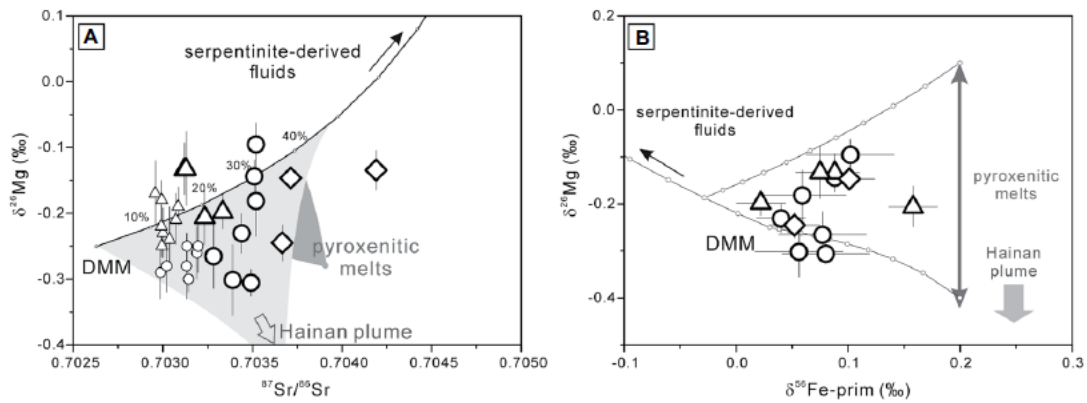
Figure 1. (A) $\delta^{26}Mg$ vs. $^{87}Sr/^{86}Sr$ and (B) $\delta^{26}Mg$ vs. $\delta^{56}Fe$-prim in the South China Sea basalts in comparison to the mixing trends between depleted MORB mantle (DMM, where MORB is mid-ocean-ridge basalt), serpentinite-derived fluids, and/or Hainan plume.

5. 水文气候的变化在过去的 5 万年里是控制非洲北部火灾活动的主要因素

翻译人：杨会会 11849590@mail.sustech.edu.cn

摘要：北非有一些地球上最常被烧毁的生物群落，包括半干旱的 Sahel 草原和南边更湿润的稀树草原。自然火灾是由雨季快速增加的生物产量、旱季干燥和频繁的干雷引起火种导致的。如今，在 Sahel 北部和南部的火灾活动明显减少，在北部是因为那里的降雨量极低，几乎消除了撒哈拉地区的生物产量，而在南部地区，森林生物群落因为太湿而无法燃烧。在上一个冰期旋回中，北非地区的降水和植被覆盖变化显著，响应于天文驱动的日照的逐步变化、大气二氧化碳水平，以及与经向翻转环流(MOC)重组相关的北大西洋突然降温事件。本文中我们报告了一项研究结果，研究这些气候变化对非洲北部过去 5 万年(50 kyr)的火灾活动的影响。我们的重建结果来自海洋沉积物，具有很强的年龄控制能力，提供了从非洲大陆排出的木炭颗粒的连续记录。我们研究了沿西北非洲边缘21 至 9°N 之间的纬度带上的三个地点。我们的研究点位显示出降雨变化和火灾活动在过去呈现出明显的纬度关系。在最南端的站点(GeoB9528-3, 9°N)，火灾活动随着湿度的增加而减少，而我们最北端的站点(ODP site 658, 21°N)则明显揭示出相反的关系。我们研究的中部站点位于今天 Sahel 南部的海上(GeoB9508-5, 15°N)，在火灾活动和水文气候之间呈现出"适居"关系，其中木炭通量在中等降雨气候条件下达到峰值，并在向更干旱或更湿润的条件过渡时受到抑制。我们的结果与概念性宏观生态模型中提出的"中间火灾生产力假设"的预测惊人地一致，并得到了现代火灾活动的经验证据的支持。火灾、气候和植被之间的反馈过程无疑是复杂的，但温度可能是全球火灾活动时间变化的主要驱动因素，而降水-蒸发平衡可能是全新世热带地区的次要影响因素。 但是，在这些解释所依据的综合记录中，非洲的情况很少。我们的结论是，在全新世(至少 50 ka)之前，水文气候(而不是温度)对北非热带地区的火灾起着主导作用。

ABSTRACT: North Africa features some of the most frequently burnt biomes on Earth, including the semi-arid grasslands of the Sahel and wetter savannas immediately to the south. Natural fires are fuelled by rapid biomass production during the wet season, its desiccation during the dry season and ignition by frequent dry lightning strikes. Today, fire activity decreases markedly both to the north of the Sahel, where rainfall is extremely low, almost eliminating biomass over the Sahara, and to the south where forest biomes are too wet to burn. Over the last glacial cycle, rainfall and vegetation cover over northern Africa varied dramatically in response to gradual astronomically-forced insolation change, changes in atmospheric carbon dioxide levels, and abrupt cooling events over the North Atlantic Ocean associated with the reorganization of Meridional Overturning Circulation (MOC). Here we report the results of a study into the impact of these climate changes on fire activity in northern African over the last 50,000 years (50 kyr). Our reconstructions come from marine sediments with strong age control that provide an uninterrupted record of charcoal particles exported from the African continent. We studied three sites on a latitudinal transect along the northwest African margin between 21 and 9°N. Our sites exhibit a distinct latitudinal relationship between past changes in rainfall and fire activity. At the southernmost site (GeoB9528-3, 9°N), fire activity decreased during intervals of increasing humidity, while our northernmost site (ODP Site 658, 21°N) clearly demonstrates the opposite relationship. The site in the middle of our transect, offshore of the present day southern Sahel today (GeoB9508-5, 15°N), exhibits a "Goldilocks" relationship between fire activity and hydroclimate, wherein charcoal fluxes peak under intermediate rainfall climate conditions and are supressed by transition to more arid or more humid conditions. Our results are remarkably consistent with the predictions of the intermediate fire productivity hypothesis developed in conceptual macroecological models and supported by empirical evidence of modern day fire activity. Feedback processes operating between fire, climate and vegetation are undoubtedly complex but temperature is suggested to be the main driver of temporal change in fire activity globally, with the precipitation-evaporation balance perhaps a secondary influence in the Holocene tropics. However, there is only sparse coverage of Africa in the composite records upon which those interpretations are based. We conclude that hydroclimate (not temperature) exerted the dominant control on burning in the tropics of northern Africa well before the Holocene (from at least 50 ka).
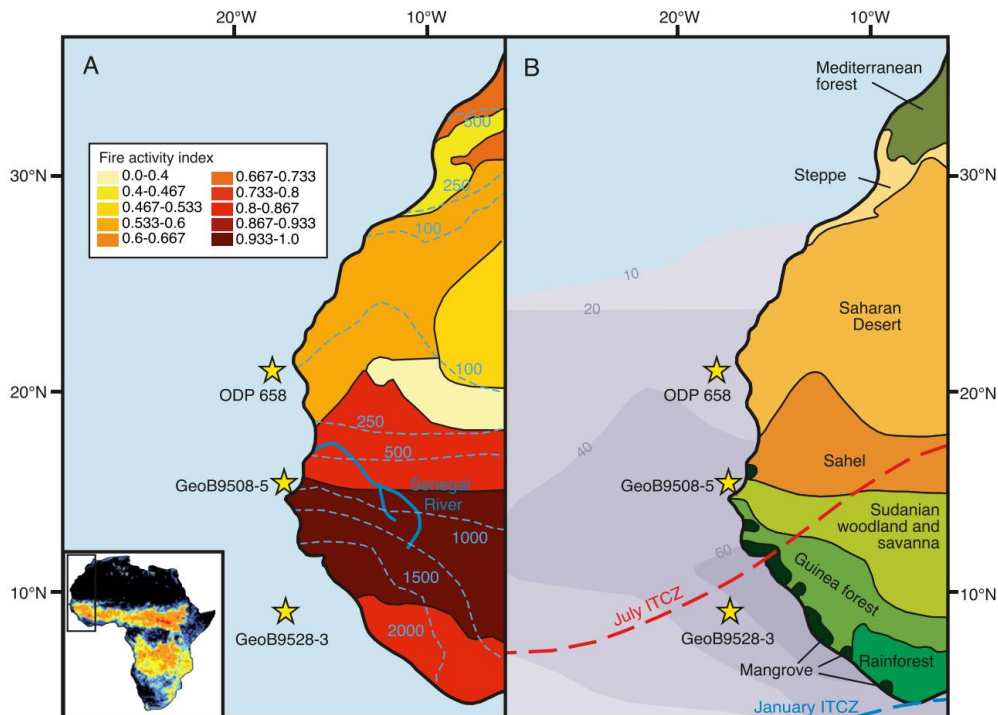
Figure 1. Our latitudinal transect of study sites: ODP 658 (21°N), GeoB9508-5 (15°N) and GeoB9528-3 (9°N). (A) Fire Activity Index, indicating the average number of fire incidents per unit area, rescaled onto a global scale of 0e1 (redrawn from Pausas and Ribeiro, 2013) and present day mean annual precipitation contours (from Larrasoana et al., 2013). Inset shows study area marked onto pan-African annual average number of fires estimated by MODIS, with hot colors indicating the highest fire incidences (image from Bowman et al., 2009; data from Giglio et al., 2006) with area covered in the main figure indicated. (B) Schematic showing the major North African vegetation bands (adapted from Hooghiemstra and Agwu, 1986; Kuechler et al., 2013) with the modern mean summer and winter latitudinal position of the ITCZ (Yan, 2005). Purple shading indicates 2007-2016 average annual dust fluxes (in mm m^{-2} day^{-1}) estimated using Infrared Atmospheric Sounding Interferometer (Yu et al., 2019). (For interpretation of the references to color in this figure legend, the reader is referred to the Web version of this article.)
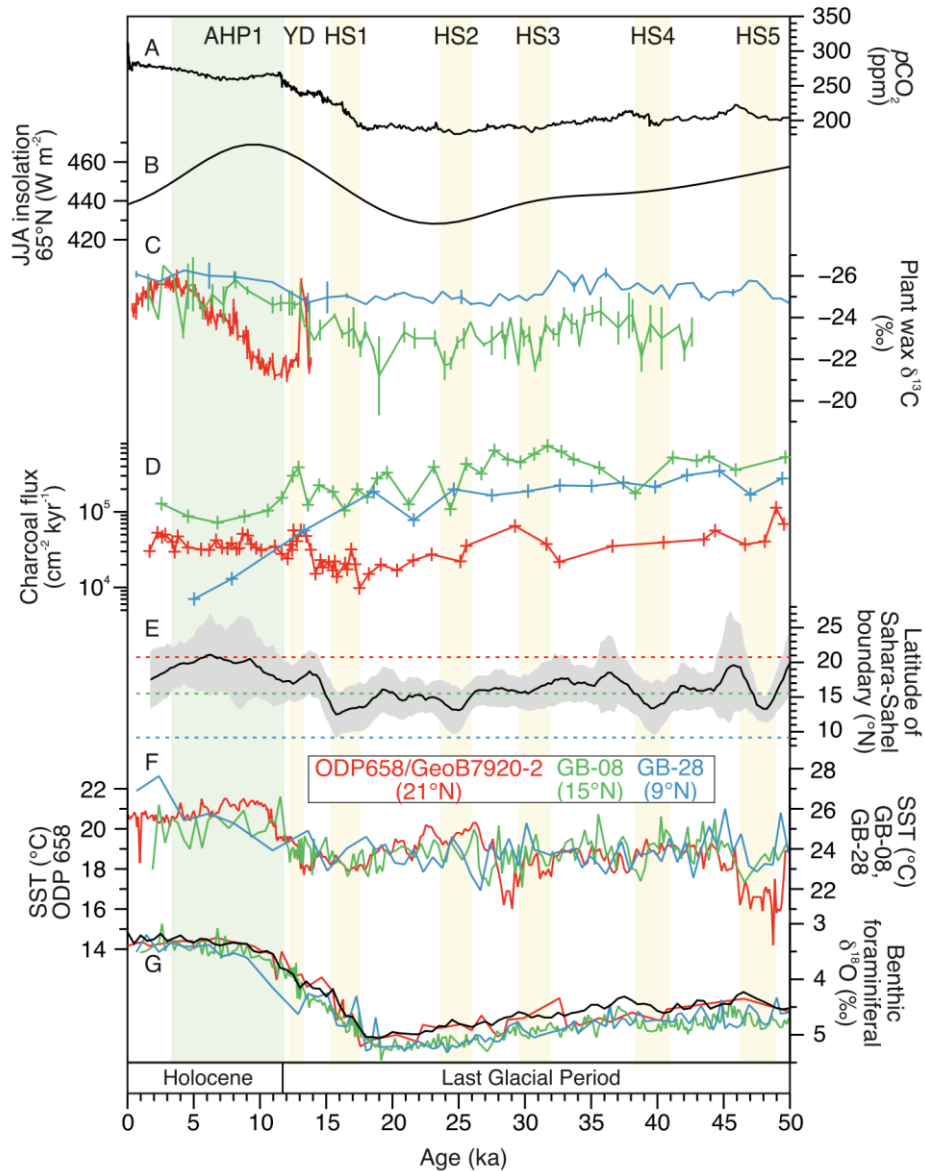
Figure 2. Comparison of fire and vegetation changes along the Northwest African Margin Transect to global climate records. Data from ODP 658 and nearby site GeoB7920-2 shown in red, GB-08 in green and GB-28 in blue. a) Atmospheric pCO_2 from a composite Antarctic ice core record (Bereiter et al., 2015 and references therein). b) Mean boreal summer insolation (June-August) at 65° N given by the La2004 orbital solution (Laskar et al., 2004). c) $\delta^{13}C$ signatures of plant waxes (C31 n-alkanes) from GeoB7920-2 (red, Dupont and Schefuß, 2018), GB-08 (green, Niedermeyer et al., 2010) and GB-28 (blue, Castaneda et al., 2009). Error bars indicate 1 standard deviation. d) Charcoal flux at ODP 658 (red), GB-08 (green) and GB-28 (blue) (this study). Note logarithmic scale on y-axis. e) Reconstructed latitude of the Sahara-Sahel boundary (five-point running average) based upon major element compositions of marine sediment, with 68% confidence interval plotted

(Collins et al., 2013a). Horizontal lines mark the latitudes of ODP 658 (red), GB-08 (green) and GB-28 (blue). f) Sea surface temperature reconstructions from ODP 658 (red, alkenone-derived, Zhao et al., 1995), GB-08 (green, from foraminiferal Mg/Ca, Zarriess et al., 2011), GB- 28 (blue, alkenone-derived, Lopes dos Santos et al., 2010). g) Benthic oxygen isotope values from ODP 658 (red, Sarnthein and Tiedemann, 1990), GB-08 (green, Mulitza et al., 2008b), GB-28 (blue, Castaneda et al., 2009) and deep North Atlantic stack (black, Lisiecki and Stern, 2016). Values from the three African margin sites have been adjusted by þ 0.64‰ to correct for species-specific offsets from isotopic equilibrium. High $\delta^{18}O$ values indicate large global ice volumes and cold bottom water temperature. (For interpretation of the references to color in this figure legend, the reader is referred to the Web version of this article.)

6. 厌氧光合铁氧化菌 *Rhodobacter ferrooxidans* SW2 的铁同位素分馏特征

翻译人：王敦繁 Dunfan-w@foxmail.com

摘要： 微生物介导的铁氧化是现今和早期地球上铁氧化还原循环的重要途径之一。该过程被认为在大氧化事件(GOE)前缺氧海洋条件下参与铁建造沉积的形成。铁同位素记录为古海洋中铁的氧化还原状态提供了重要的档案资料。已有许多利用不同代谢途径的细菌进行铁氧化实验。然而，在厌氧光合铁氧化过程中，Fe 同位素的分馏方式和分馏程度，以及其对古海洋铁库氧化还原状态的意义仍需进一步研究。在这里，我们报道了在环境温度(20℃)下，由无氧光营养铁氧化红杆菌(*Rhodobacter ferrooxidans* SW2)产生的 Fe(II)aq 和 Fe(III) (oxyhydr)氧化物沉淀之间的 Fe 同位素分馏。莫斯鲍尔谱分析表明，其最终产物为水合铁。Fe(II)aq 与沉淀矿物($\Delta^{56}Fe_{precipitate-Fe (II)aq}$)校正后的 Fe 同位素分馏值为:培养 1 天后约-0.37±0.04‰(2se, N = 2)，培养 22 天后约 2.96±0.17‰(2se, N = 2)。观察到的分馏现象既不能用简单的瑞利过程解释，也不能用平衡过程解释，但很可能记录了在 22 天的栽培期间，同位素不平衡达到完全或接近完全平衡的过程。相比动力学效应，7 天后较低的析出速率、较小的氧化产物和溶解-氧化-再析出过程可能主导了同位素交换，导致析出相与 Fe(II)aq 之间的最终同位素平衡。研究结果表明，铁元素在该无氧光合铁氧化菌作用下生成的水铁矿相对容易达到铁同位素平衡，因此含铁矿物铁同位素的形成可能与其沉淀环境中的流体有关，比如有些情况下仅来自太古宙海水。

ABSTRACT: Microbially mediated Fe(II) oxidation is one of the most important pathways of Fe redox cycling on both present and early Earth. It was proposed to participate in iron formations (IFs) deposition under oxygen-depleted oceanic conditions before the Great Oxidation Event (GOE). Fe isotopic records in IFs provide important archives for the redox state of iron pool in paleo oceans. There have been a number of iron-oxidizing experiments which used bacteria with different metabolic pathways. However, it still needs further research on how and to what extent Fe isotopes

are fractionated during Fe(II) oxidation mediated by the anoxygenic phototrophic Fe(II)-oxidizer, as well as its implications for the redox state of iron pool in paleo oceans. Here, we report Fe isotope fractionation between Fe(II)aq and Fe(III) (oxyhydr)oxides precipitates produced by the anoxygenic phototrophic Fe(II)-oxidizer *Rhodobacter ferrooxidans* SW2 at ambient temperature (20°C). Mössbauer spectroscopy analyses indicated that the final mineral product was ferrihydrite. The corrected Fe isotope fractionation between Fe(II)aq and precipitates ($\Delta^{56}Fe_{precipitate-Fe(II)aq}$) ranged from ca. -0.37 ± 0.04‰ (2se, N = 2) after 1 day of cultivation to 2.96 ± 0.17‰ (2se, N = 2) after 22 days of cultivation. The observed fractionation cannot be explained by neither a simple Rayleigh nor equilibrium process, but likely recorded a process from an isotopic disequilibrium reaching complete or near-complete equilibrium during 22 days of cultivation. The lower precipitation rate after 7 days, small size of oxidation products and dissolution-oxidation-reprecipitation processes probably promoted isotope exchange overwhelming the kinetic effect, resulting in a final isotope equilibrium between precipitates and Fe(II)aq. It revealed that the ferrihydrite produced by Fe(II) oxidation by anoxygenic photoferrotrophy could reach Fe isotope equilibrium relatively easily, thus iron formation may record Fe isotope equilibrium with the fluids from which they precipitated, i.e. in some cases solely from seawater in Archean oceans.
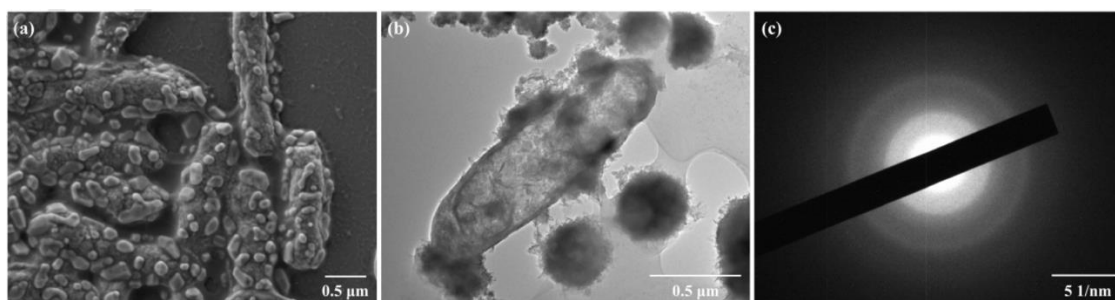
Figure 1. Scanning (a) and transmission (b) electron micrographs of *R. ferrooxidans* SW2 and its final mineral products. A selected area electron diffraction (SAED) pattern for the final mineral products (c).

7. 阿黎凡特晚第四纪水气候：来自死海的叶蜡记录

翻译人：王浩森 11930841@mail.sustech.edu.cn

摘要：随着温室气体排放量的增加，东地中海预计将经历干旱和极端降雨情况的增加。该地区的古气候记录对于进一步限制水循环对全球变暖气候的响应至关重要。其中，死海深度钻井项目（DSDDP）收集的死海湖泊记录提供了过去 20 万年气候变化的历史，并记录了区域水平衡的巨大变化。在这里，我们分析了 DSDDP 5017-1 上的叶蜡同位素（δD_{wax}，$\delta^{13}Cwax$），并将结果与同一岩芯上分析的其他指标进行了比较。δD_{wax} 记录与附近 Soreq 洞穴的 $\delta^{18}O$ 记录非常相似，表明两者都记录了冰期-间冰期周期的区域一致性特征以及冬季降雨与亚非季风系统大规模扩张和收缩之间的相互作用。花粉和岩芯岩性的主成分分析表明，死海古气候记录变化的一阶驱动力是全球温度，它通过调节大气蒸发需求来控制有效湿度。叶蜡、花粉和岩芯岩性都表明，在最后一次间冰期的峰值期间，降水的年周期发生了根本变化。我们假设死海盆地在此期间经历了双重降雨机制，即冬季风暴加剧，夏季季风季节。虽然这些变化是由地球的进动周期驱动的，但模型的模拟表明，在二氧化碳水平升高的情况下，非洲季风区域也会类似地扩展到阿拉伯半岛。DSB 的最后一次间冰期气候提供了地中海东南部地区未来气候的参考。

ABSTRACT: The eastern Mediterranean is projected to experience increases in drought and extreme rainfall in response to rising greenhouse gas emissions. Paleoclimate records from this region are crucial to further constrain the response of the water cycle to a globally warmer climate. Of these, the Dead Sea lacustrine record, collected by the Dead Sea Deep Drilling Project (DSDDP), provides a detailed history of climate change over the past 200,000 years and documents large-magnitude changes in regional water balance. Here, we analyze leaf wax isotopes (δD_{wax}, $\delta^{13}C_{wax}$) on DSDDP 5017-1 and compare results to other proxies analyzed on the same core. The $\delta Dwax$

record closely resembles the speleothem $\delta^{18}O$ record from nearby Soreq Cave, suggesting that both record a regionally coherent signature of glacial-interglacial cycles and the interplay between winter season rainfall and large-scale expansion and contraction of the Afro-Asian monsoon system. Principal components analysis of the pollen and core lithology shows that the first-order driver of variability in the Dead Sea paleoclimate record is global temperature, which controls effective moisture by modulating atmospheric evaporative demand. Leaf wax, pollen, and core lithology all suggest radical changes in the annual cycle of precipitation during the peak of the Last Interglacial. We hypothesize that the Dead Sea Basin experienced a dual-rainfall regime during this time, with intensified winter storms and a summer monsoon season. While these changes were driven by the Earth's precessional cycle, model simulations suggest a similar expansion of the African monsoon domain into the Arabian Peninsula under elevated CO_2 levels. The Last Interglacial climate of the DSB provides a glimpse of what future climate in the southeastern Mediterranean region could look like.
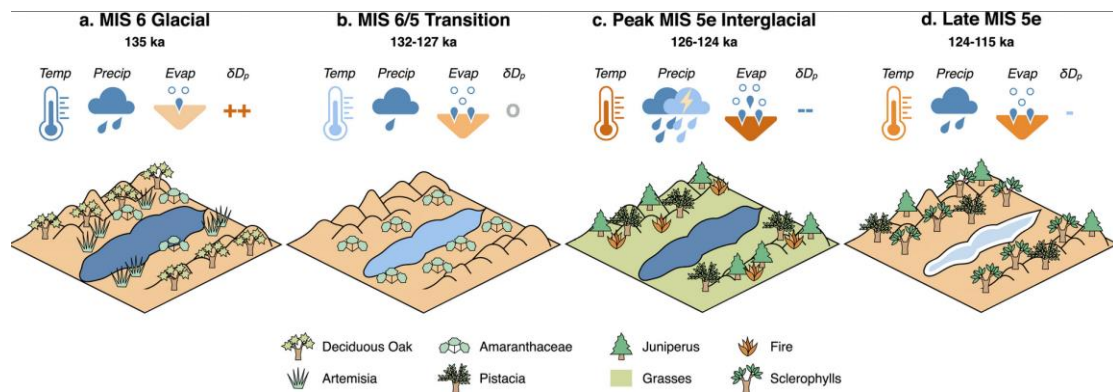
Figure 1. Schematic of climate and environmental changes through MIS 5e in the Dead Sea Basin based on leaf wax isotopes, pollen, and lake levels.

8. 海底文石溶解保护方解石

翻译人：曹伟 11930854@qq.com

摘要： 在开阔的海洋中，碳酸钙主要以两种矿物形式存在。溶解度最低的方解石在海底广泛存在，而溶解度较高的文石则很少保存在海洋沉积物中。尽管文石的溶解度更大，但研究表明，文石对全球远洋钙化的贡献与方解石相当，可以到达深海。如果大量的文石在海底沉淀并溶解，这就代表了一个很大的碱性来源，可以作为碳酸盐镀层在深海中缓冲，并且有利于保存较难溶解的方解石。本研究中，我们使用一种新型的三维纳米尺度反应传输模型，结合天然文石和方解石壳层的三维 x 射线断层扫描结构，研究了文石溶解对富方解石沉积物早期成岩作用的影响。结果与最近的研究成果一致，强调了扩散运输在海底碳酸钙溶解过程中的重要作用。结果表明，文石在海底的局部通量足以抑制海底表层方解石的溶解，可能造成方解石重结晶。由于文石的产生特别容易受到海洋酸化的影响，未来文石的镀层效果可能会减弱，而沉积物-水界面的方解石溶解将不得不覆盖更大份额的二氧化碳中和作用。

ABSTRACT: In the open ocean, calcium carbonates are mainly found in two mineral forms. Calcite, the least soluble, is widespread at the seafloor, while aragonite, the more soluble, is rarely preserved in marine sediments. Despite its greater solubility, research has shown that aragonite, whose contribution to global pelagic calcification could be at par with that of calcite, is able to reach the deep-ocean. If large quantities of aragonite settle and dissolve at the seafloor, this represents a large source of alkalinity that buffers the deep ocean and favours the preservation of less soluble calcite, acting as a deep-sea, carbonate version of galvanization. Here, we investigate the role of aragonite dissolution on the early diagenesis of calcite-rich sediments using a novel 3D, micrometric-scale reactive-transport model combined with 3D, X-ray tomography structures of natural aragonite and calcite shells. Results highlight the important role of diffusive transport in benthic calcium carbonate dissolution, in agreement with recent work. We show that, locally, aragonite fluxes to the seafloor

could be sufficient to suppress calcite dissolution in the top layer of the seabed, possibly causing calcite recrystallization. As aragonite producers are particularly vulnerable to ocean acidification, the proposed galvanizing effect of aragonite could be weakened in the future, and calcite dissolution at the sediment-water interface will have to cover a greater share of CO_2 neutralization.
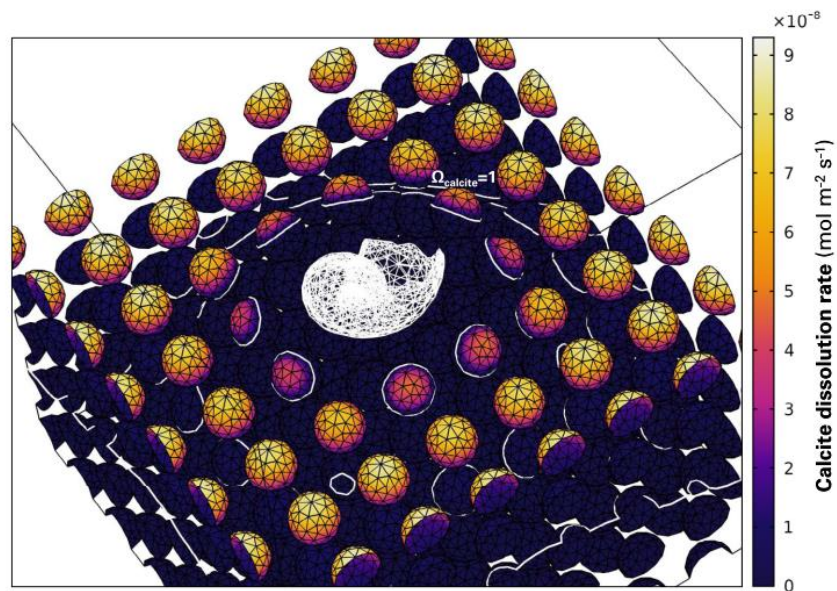
Figure 1. Dissolution of calcite grains in a sediment bed capped with a dissolving aragonite pteropod.

9. 定量地球的放射性热

翻译人：张伟杰 12031188@mail.sustech.edu.cn

摘要: 瓜德地球内部的热量驱动着它的动力引擎，并形成地幔对流、板块构造和地球发电机。这些使地球适合居住的更新和保护过程是由原始和放射热维持的。在过去的二十年里，粒子物理学家测量了地中微子的通量，即在 β^- 衰变过程中发射的电子反中微子。这些幽灵般的粒子直接测量了地球上的产热元素（HPE: Th & U）的数量，进而确定了地球上难熔元素的绝对浓度。地中微子通量有来自岩石圈和地幔的贡献。探测器灵敏度遵循 $1/r^2$（源探测器分离距离）依赖性。因此，需要一个围绕每个实验的近场岩石圈（NFL，最近 500 公里）的准确地质模型来定义地幔的贡献。由于接近探测器和富集 HPEs，如果当地岩石圈贡献了约 50% 的信号对解释地幔信号的影响最大。我们重新分析了 Agostini 等（2020）在 Borexino 实验中使用的上地壳组成模型。我们调查了西部近场区域的地质情况，发现富含钾质火山活动，包括一些距离探测器 50 公里以内的中心区域。相比之下，Agostini 的研究没有包括这些岩性，对于 Borexino 实验周围 150 公里的上地壳岩石只使用了 HEP 低、富含碳酸盐的模型。因此，我们报告了当地上地壳>3 倍的 U 含量，与他们的研究相比本研究显示地球放射性热量相应有 200%的减少。KamLAND 和 Borexino 地中微子实验的结果相互矛盾，预测地幔成分的异质性是不可靠的。使用我们修正的局部模型对 KamLAND 和 Borexino 实验的综合分析指示地球的总放射源功率为目前为每天~ 20 TW。下一代地球中微子探测器（SNO+，计数;以及正在建设中的 JUNO）将更好地约束地球的 HPE。

ABSTRACT: The Earth's internal heat drives its dynamic engine, causing mantle convection, plate tectonics, and the geodynamo. These renewing and protective processes, which make Earth habitable, are fueled by primordial and radiogenic heat. For the past two decades, particle physicists have measured the flux of geoneutrinos, electron antineutrinos emitted during β^- decay. These ghost-like particles provide a direct measure of the amount of heat producing elements (HPE: Th &

U) in the Earth and in turn define the planet's absolute concentration of the refractory elements. The geoneutrino flux has contributions from the lithosphere and mantle. Detector sensitivity follows a $1/r^2$ (source detector separation distance) dependence. Accordingly, an accurate geologic model of the Near-Field Lithosphere (NFL, closest 500 km) surrounding each experiment is required to define the mantle's contribution. Because of its proximity to the detector and enrichment in HPEs, the local lithosphere contributes ∼50% of the signal and has the greatest effect on interpreting the mantle's signal. We re-analyzed the upper crustal compositional model used by Agostini et al. (2020) for the Borexino experiment. We documented the geology of the western Near-Field region as rich in potassic volcanism, including some centers within 50 km of the detector. In contrast, the Agostini study did not include these lithologies and used only a HPE-poor, carbonate-rich, model for upper crustal rocks in the surrounding ∼150 km of the Borexino experiment. Consequently, we report 3× higher U content for the local upper crust, which produces a 200% decrease in Earth's radiogenic heat budget, when compared to their study. Results from the KamLAND and Borexino geoneutrino experiments are at odds with one another and predict mantle compositional heterogeneity that is untenable. Combined analyses of the KamLAND and Borexino experiments using our revised local models strongly favor an Earth with ∼20 TW present-day total radiogenic power. The next generation of geoneutrino detectors (SNO+, counting; and JUNO, under construction) will better constrain the HPE budget of the Earth.
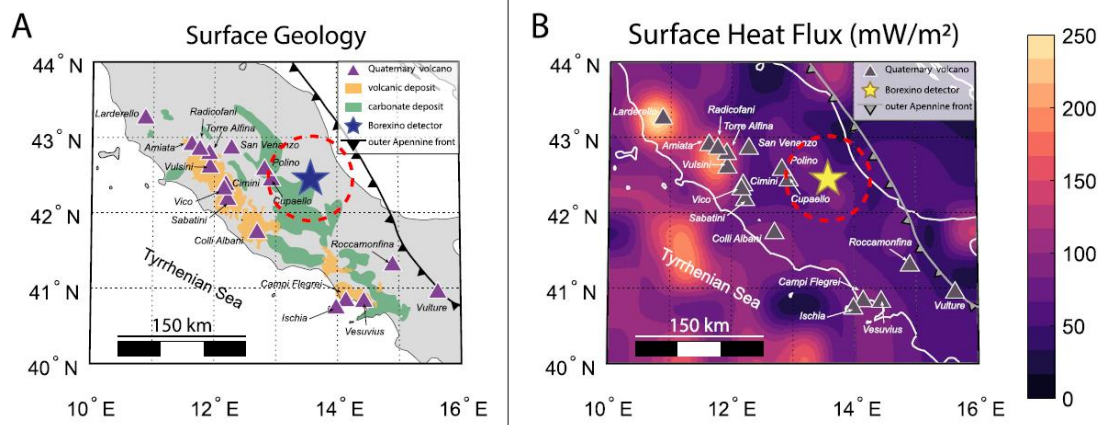
Figure 1. A simplified geological map (A) of the central Italian peninsula showing extensive volcanism on the western portion and carbonate platforms to the east (modified after Cosentino et al. (2010); Conticelli et al. (2007)). The red dashed line circles the Borexino detector (blue star) at a radius of 50 km. Quaternary volcanic deposits in the west coincide with high surface heat flux (B). Heat flux data from Lucazeau (2019).

10. 东地中海和中东的气候变化和极端天气

翻译人：李海 12031330@mail.sustech.edu.cn

摘要：基于观测和模拟的研究已将东地中海和中东（EMME）地区确定为一个突出的气候变化热点。虽然有几项举措已经解决了气候变化在部分 EMME 地区的影响，但作者提出了一项更新的评估，涵盖了广泛的时间尺度、现象和未来路径。作者的评估基于对近期观察和预测的修订分析以及对近期关于区域气候变化原因和影响的科学文献的广泛概述。EMME 的温室气体排放量增长迅速，超过了欧盟，因此对气候变化做出了重大贡献。在过去的半个世纪里，尤其是最近几十年里，EMME 的变暖速度明显快于其他有人居住的地区。与此同时，水循环的变化也变得明显。预计最近观察到的每十年约 0.45℃的气温上升仍将继续，尽管全球温室气体排放的大幅减少会缓和这一趋势。除了预计的平均气候条件的变化外，作者还呼吁关注具有潜在破坏性社会影响的极端天气事件。其中包括热浪、干旱和沙尘暴以及可能引发山洪暴雨事件的严重程度和持续时间都在急剧增加。本文还讨论了该地区的大气污染和土地利用变化，包括城市化、荒漠化和森林火灾。最后，作者确定可能受到严重影响的部门，并制定适应和研究建议，以提高 EMME 对气候变化的适应能力。

ABSTRACT: Observation-based and modelling studies have identified the Eastern Mediterranean and Middle East (EMME) region as a prominent climate change hotspot. While several initiatives have addressed the impacts of climate change in parts of the EMME, here we present an updated assessment, covering a wide range of timescales, phenomena and future pathways. Our assessment is based on a revised analysis of recent observations and projections and an extensive overview of the recent scientific literature on the causes and effects of regional climate change. Greenhouse gas emissions in the EMME are growing rapidly, surpassing those of the European Union, hence contributing significantly to climate change. Over the past half-century and especially during recent

decades, the EMME has warmed significantly faster than other inhabited regions. At the same time, changes in the hydrological cycle have become evident. The observed recent temperature increase of about 0.45°C per decade is projected to continue, although strong global greenhouse gas emission reductions could moderate this trend. In addition to projected changes in mean climate conditions, we call attention to extreme weather events with potentially disruptive societal impacts. These include the strongly increasing severity and duration of heatwaves, droughts and dust storms, as well as torrential rain events that can trigger flash floods. Our review is complemented by a discussion of atmospheric pollution and land-use change in the region, including urbanization, desertification and forest fires. Finally, we identify sectors that may be critically affected and formulate adaptation and research recommendations towards greater resilience of the EMME to climate change.
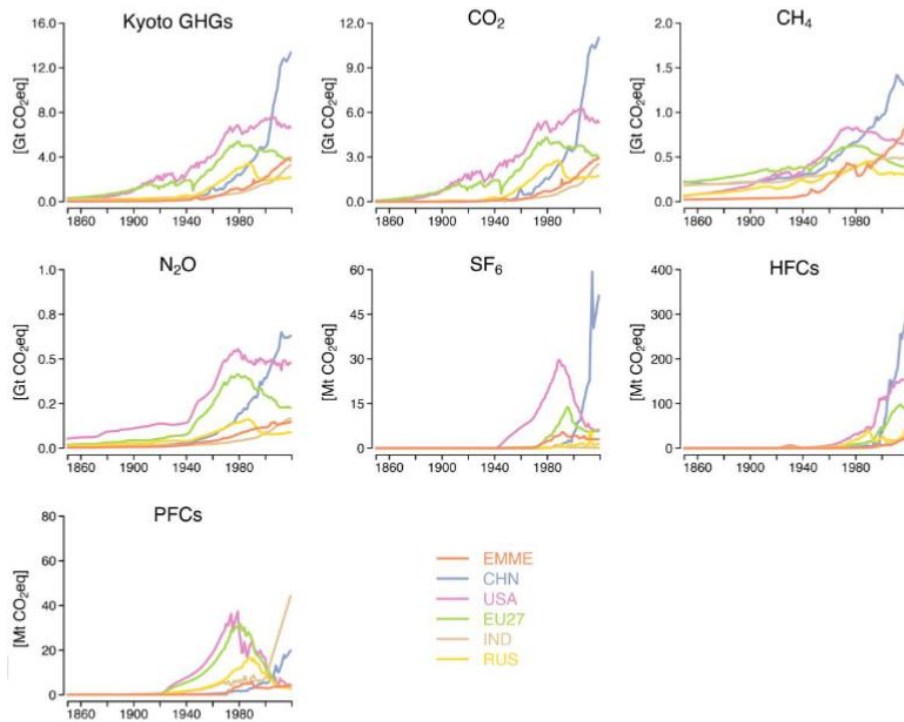
Figure 1. Historical emissions of greenhouse gases across selected countries and regions (EMME = Eastern Mediterranean and Middle East; CHN = China; USA = United States of America; EU27 = European Union; IND = India; RUS = Russia; OTHERS = other countries). Data sources: country reported (HISTCR) emissions from the PRIMAP-hist dataset version 2.3.1 (Gütschow et al., 2016; 2021).
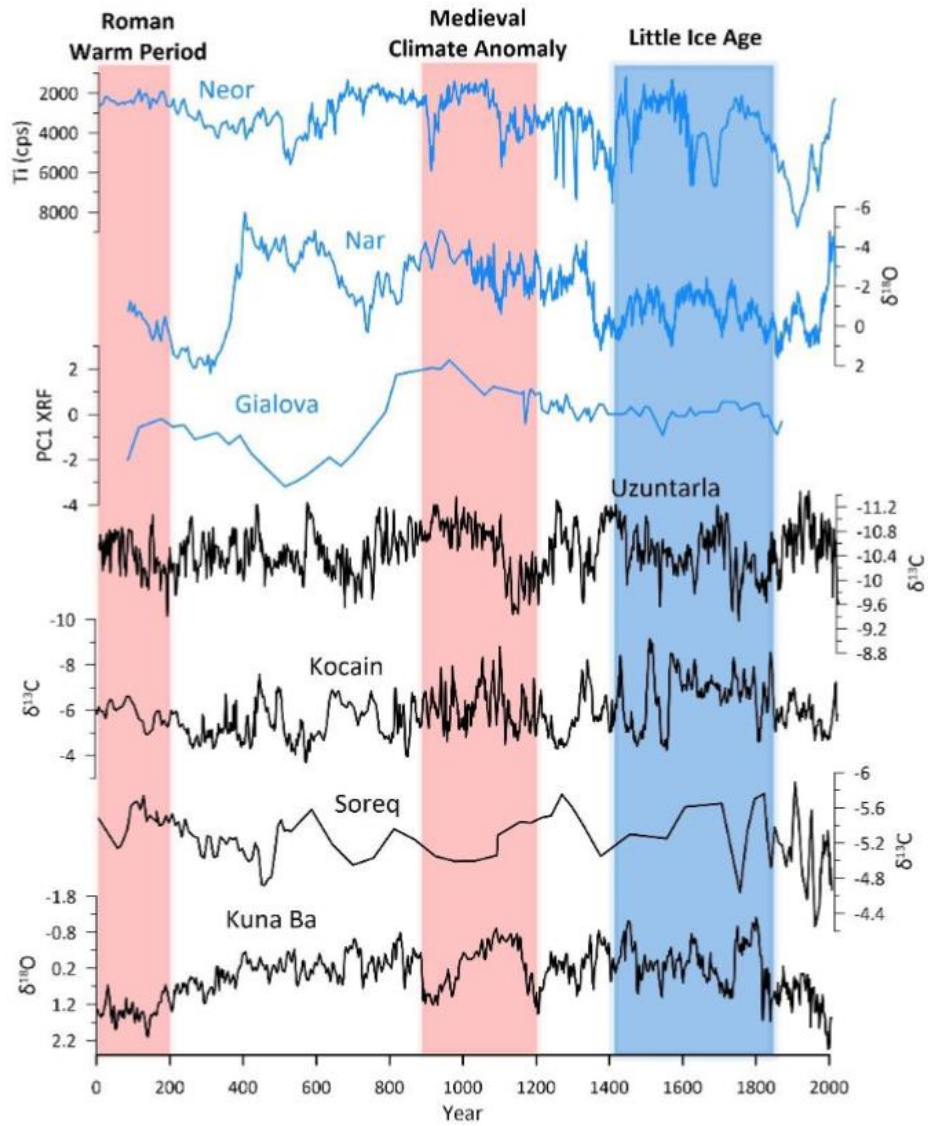
Figure 2. Regional hydroclimate proxy records of the past 2000 years (source: Luterbacher and Xoplaki, 2019; Xoplaki et al. 2021, updated).

11. 周期性古地磁异常揭示了南大西洋磁异常的未来演变

翻译人：刘宇星 11811211@mail.sustech.edu.cn

摘要：在过去的两个世纪中，地磁场的强度迅速下降，同时南大西洋出现了磁场异常的不对称增长。但地磁场下降的内在过程存在争议，这导致人们猜测地磁场可能即将逆转。在这里，我们提出了一个基于过去 9000 年间接观测的地磁场模型，并确定了模型中的古地磁类比。该模型是使用概率方法构建的，该方法解决了阻碍先前尝试中的年龄不确定和沉积数据平滑问题。我们发现了与偶极矩千年尺度周期变化有关的反复出现的半球场不对称的证据。我们的重建表明偶极矩的最小值往往与地磁场异常一致，类似于南大西洋异常。我们提出，以强烈不对称场为特征的公元 600 年左右的时期可以提供与当今磁场的类比。这个类比意味着南大西洋异常可能会在接下来的几百年内消失，回归到更对称的场配置，并且可能会加强轴向偶极场。

ABSTRACT: The strength of the geomagnetic field has decreased rapidly over the past two centuries, coinciding with an increasing field asymmetry due to the growth of the South Atlantic Anomaly. The underlying processes causing the decrease are debated, which has led to speculation that the field is about to reverse. Here, we present a geomagnetic field model based on indirect observations over the past 9,000 y and identify potential ancient analogs. The model is constructed using a probabilistic approach that addresses problems with age uncertainties and smoothing of sedimentary data that have hampered previous attempts. We find evidence for recurrent hemispherical field asymmetries, related to quasiperiodic millennial-scale variations in the dipole moment. Our reconstruction indicates that minima in the dipole moment tend to coincide with geomagnetic field anomalies, similar to the South Atlantic Anomaly. We propose that the period around 600 BCE, characterized by a strongly asymmetric field, could provide an analog to the

present-day field. The analogy implies that the South Atlantic Anomaly will likely disappear in next few hundred years, accompanied by a return to a more symmetric field configuration and possibly, a strengthening of the axial dipole field.
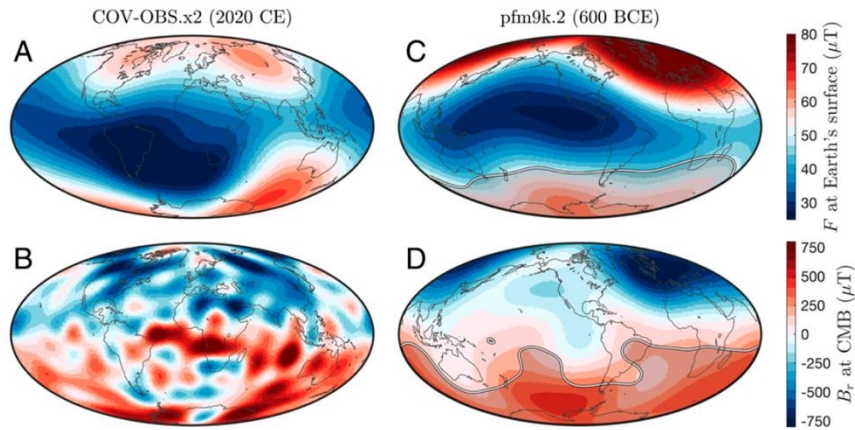
Figure 1. Maps of geomagnetic field intensity (F) at Earth's surface and radial field (Br) at the CMB based on model averages of (A and B) COV-OBS.x2 at 2020 CE and (C and D) pfm9k.2 at 600 BCE. The geomagnetic field at 600 BCE serves as a potential ancient analog to the present. The projection in B and D maps (600 BCE) has been rotated 100∘ toward the east to align the eccentric dipole axis location with A and C (red star in Fig. 2B). (C and D) Gray shaded areas, which represent regions where the model SD exceeds 5 and 120 µT, respectively, are added to highlight the large model uncertainties, particularly in the Southern Hemisphere field predictions. Movies S1 and S2 have more detailed information on the model uncertainties.
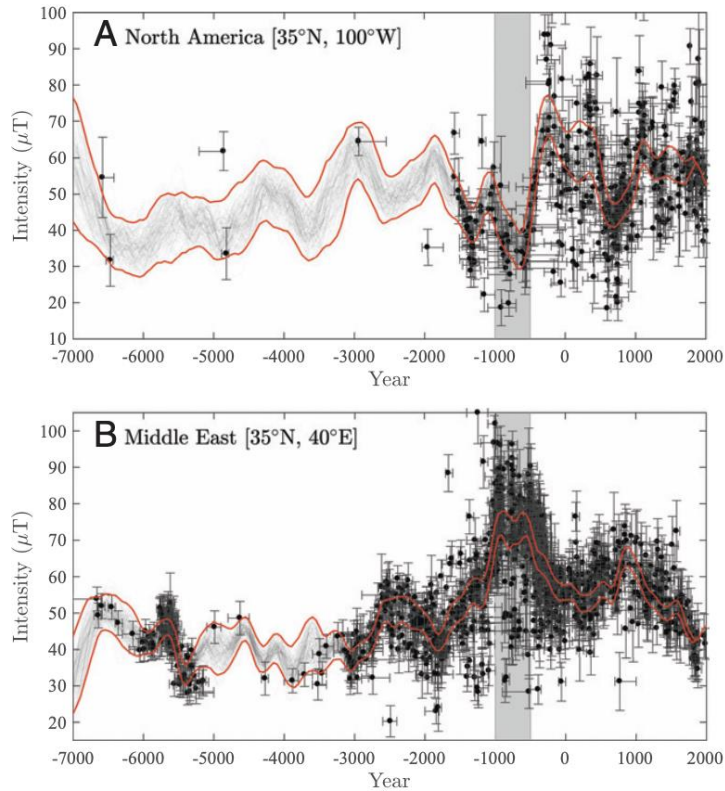
Figure 2. Model–data comparison of variations in geomagnetic field intensity over the past 9,000 y in (A) North America and (B) the Middle East. The vertical gray shaded bands between 1000 and 500 BCE are added to highlight the large Northern Hemisphere asymmetry in the field during this time. Model predictions are represented by 100 samples from the posterior distribution (semitransparent black lines) and the 95% credible intervals (red lines). The archeomagnetic data (black dots; plotted on the maximum posterior probability ages) were selected from radii of 30◦ and 10◦, respectively, and relocated assuming an axial dipole field. The large radii used to select the data, chosen to obtain a reasonable amount of data for the comparison, can be justified on account that the model resolution is limited to spherical harmonic degree 5 (i.e., spatial wavelengths of 72◦). Error bars represent 1-σ uncertainties. Note that the y-axes limits have been adjusted to highlight the main features of the field variation, thereby omitting four and three unusually high-intensity data, respectively.